

Rational Passivation of Sulfur Vacancy Defects in Two-Dimensional Transition Metal Dichalcogenides

Hope Bretscher,[†] Zhaojun Li,^{†,‡} James Xiao,[†] Diana Yuan Qiu,[¶] Sivan Refaely-Abramson,[§] Jack A. Alexander-Webber,[†] Arelo Tanoh,[†] Ye Fan,[†] Géraud Delport,[†] Cyan A. Williams,[†] Samuel D. Stranks,[†] Stephan Hofmann,[†] Jeffrey B. Neaton,^{||,⊥} Steven G. Louie,^{||,⊥} and Akshay Rao^{*,†}

[†]*University of Cambridge, Cambridge, CB2 1TN, UK*

[‡]*Uppsala University, Uppsala, 751 20, Sweden*

[¶]*Yale University, New Haven CT, 06520, USA*

[§]*Weizmann Institute of Science, Rehovot, 76100, Israel*

^{||}*University of California Berkeley, Berkeley, CA, 94720, USA.*

[⊥]*Lawrence Berkeley National Laboratory, Berkeley, CA, 94720, USA*

E-mail: ar525@cam.ac.uk

Abstract

Structural defects vary the optoelectronic properties of monolayer transition metal dichalcogenides, leading to concerted efforts to control defect type and density *via* materials growth or post-growth passivation. Here, we explore a simple chemical treatment that allows on-off switching of low-lying, defect-localized exciton states, leading to tunable emission properties. Using steady-state and ultrafast optical spectroscopy, supported by *ab initio* calculations, we show that passivation of sulfur vacancy defects,

which act as exciton traps in monolayer MoS₂ and WS₂, allows for controllable and improved mobilities and an increase in photoluminescence up to 275-fold—more than twice the value achieved by other chemical treatments. Our findings suggest a route for simple and rational defect engineering strategies for tunable and switchable electronic and excitonic properties through passivation.

Key words: 2D materials, defects, spectroscopy, many-body perturbation theory, defect engineering, TMDC

Single and few-layer semiconducting, two-dimensional transition metal dichalcogenides (2D-TMDCs) have received significant attention in recent years due to their unique optoelectronic properties. Monolayer TMDCs possess a direct bandgap, optical excitations in the visible range, and very high absorption coefficients.^{1–3} However, the photoluminescence (PL) arising from exciton radiative recombination typically shows low PL quantum yields (PLQYs); in monolayer MoS₂ and WS₂, prepared *via* exfoliation or chemical vapor deposition, the PLQY has been measured to be below 1 % for MoS₂ and only slightly higher for WS₂.^{1,4,5} This low PLQY is attributed to the presence of defects in these materials,^{6–9} which quench photoluminescence and limit carrier mobilities.^{5,6,10–12} A systematic understanding of the nature of defects and the corresponding development of appropriate defect passivation strategies is hence greatly desired and is expected to improve device applications ranging from light-emitting diodes and photovoltaics, to quantum emitters and future quantum information devices.

Vast recent research is dedicated to identifying defect types and their effect on material functionality in monolayer TMDCs.^{9,13–20} While numerous prototypical structural defects are considered abundant, point chalcogen vacancies have been shown to have the lowest formation energy.^{21–23} Transmission electron microscopy (TEM) and scanning tunneling microscopy (STM) have been used to identify sulfur vacancies in MoS₂ and WS₂, with densities of $\sim 10^{13}$ cm⁻².^{10,23–25} These vacancies form electronic states within the bandgap, leading to the formation of low-lying defect excitons, which also form hybridized states with higher

energy, band edge excitons.¹⁸ Recent research combining scanning tunneling spectroscopy (STS), atomic force microscopy (AFM), and *ab initio* theory, suggests that oxygen substitutions at the chalcogen site – which appear nearly identical to chalcogen vacancies in TEM and AFM – are also abundant in TMDCs and are formed both during crystal growth and exposure to ambient conditions.^{16,17,26} Oxygen substitutions of this kind are not expected to possess the in-gap defect states or subgap excitonic states associated with the vacancy defect,^{16–18,22–24,26–29} and their impact on the optical signatures remains unclear. Such microscopic understanding of the electronic and excitonic states and their relation to the structure of defects suggests possible passivation pathways to control the PLQY through defect design.

A number of methods have been proposed to increase the PLQY in TMDC samples through defect passivation, including chemical treatments^{30–33} and thermal annealing.^{34,35} Despite these efforts, the magnitude of the PL increase due to such treatments is still not satisfying, and typically less than a ten-fold enhancement.^{29,32,33,36–38} A relatively successful chemical treatment for defect passivation is based on the organic superacid bis(trifluoromethane)sulfonimide (H-TFSI), which is found to increase the PL signal by orders of magnitude.⁴ Both this superacid treatment⁴ and electrical gating in a capacitive structure³⁹ increase PL *via* the same pathway, namely by reducing the high *n*-doping often found in both exfoliated and grown MoS₂ and WS₂ monolayers.^{26,40–42} These excess charges readily form trions, for which radiative recombination is much less efficient than for the neutral exciton,^{29,43,44} suggesting that excess *n*-doping may be the primary cause of low PLQY in these monolayers. It has also been shown that the PL lifetime increases upon TFSI treatment,^{45–47} which is not ideal for devices as it opens up competing channels of non-radiative decay processes. In addition, carrier mobilities are shown to be limited in TFSI-treated samples, compared to as-exfoliated samples.⁴⁷ These observations suggest that while they enhance the PL yield, such treatment may not passivate defect sites and hence does not improve defect trap-limited properties.

In this article, we explore the effect of defect passivation on PL yield and exciton life-

times in monolayer TMDCs. We study the nature of defect states created upon various chemical passivation methods through steady-state and ultrafast spectroscopy, supported by *ab initio* GW and Bethe Salpeter Equation (GW-BSE) calculations.^{48–51} We experimentally demonstrate the formation of subgap absorption features that are consistent with theoretically predicted energies for confined excitons associated with sulfur vacancies. These subgap states act as traps and lengthen PL lifetimes while limiting PL yields and carrier mobilities. We further develop a generalizable passivation protocol for sulfur vacancies, by treating samples with a passivating agent (PA), such as a thiol or sulfide, followed by a Lewis acid, such as the TFSI superacid to remove excess electrons. This two-step passivation treatment greatly enhances the measured PL, by over 275-fold from the brightest spot on untreated samples compared to the brightest spot on treated samples, and exhibit a mean enhancement of $\sim 10\times$ (Supporting Information, Table 1). The treatment further decreases the PL lifetime and improves carrier mobilities by two orders of magnitude relative to TFSI treatment alone, suggesting passivation of sulfur vacancies. The generalizability of this protocol, which can be performed with a number of chemical agents, not only enhances the optoelectronic properties of TMDCs through passivation, but can be used to functionalize these materials and tune their PL properties.

Results and Discussion

We begin by comparing the photophysical properties of as-exfoliated, (referred to as untreated), MoS₂, which is considered to be heavily *n*-doped,^{26,39–42} with a sample that was chemically treated with TFSI, where the *n*-doping has been significantly reduced (referred to as TFSI-treated). Samples are mechanically exfoliated onto Si/SiO₂ or fused silica substrates using the gold-assisted exfoliation method.⁵³ All measurements were performed at room temperature. Fig. 1a, top, compares the steady-state optical absorption spectra of untreated MoS₂, as well as TFSI-treated spectra with and without passivating agents (PA)

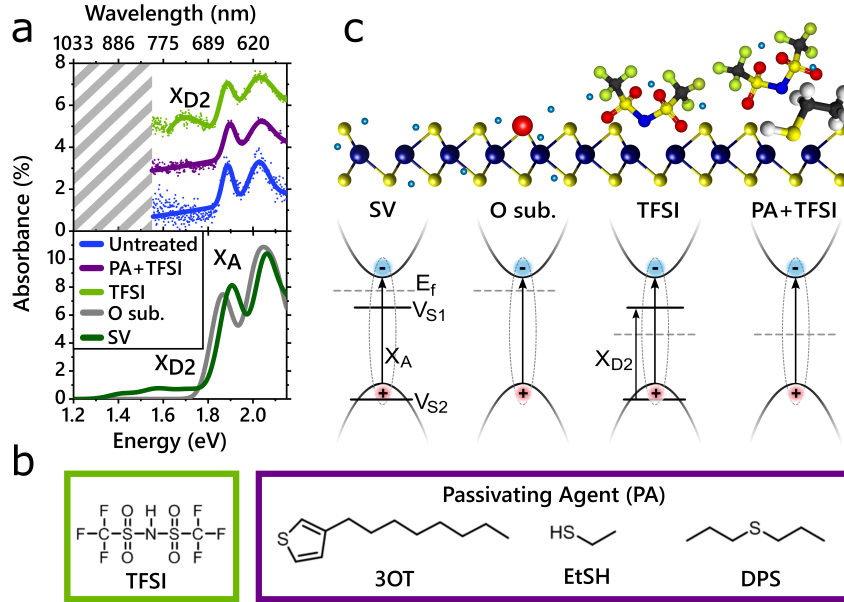


Figure 1: Absorption and treatment schematic. a) Top: Absorption of untreated (blue), TFSI-treated (green), and PA+TFSI treated (purple) monolayer MoS₂. TFSI-treated samples possess a subgap absorption peak, X_{D2} . Bottom: Calculated *ab initio* GW-BSE absorbance spectrum of monolayer MoS₂ with a 2 % sulfur vacancy density (green line) and a 2 % oxygen substitution density (grey line). X_{D2} corresponds to excitons arising from transitions between a defect level within the valance band (V_{S2}) and an in-gap defect level (V_{S1}) b) Chemical makeup of TFSI and the passivating agents used in this study. c) Ball and stick model (top) and schematic of the low-energy band structure in the K valley in MoS₂ and proposed impact of different chemical treatments outlined in (b). MoS₂ ball and stick model originally drawn in VESTA.⁵² Untreated S vacancy (SV) and untreated O substitution (O sub.) do not possess an optically accessible subgap state. In the untreated S vacancy case, the transition between the defect states (X_{D2}) is prohibited as the subgap state is occupied due to the high Fermi-level. With an oxygen substitution, there is no in-gap defect state. TFSI treatment lowers the Fermi level and may remove an oxygen substitution, which allows the defect-to-defect transition, X_{D2} , to occur. With PA+TFSI treatment, the Fermi level is lowered and the subgap state is eliminated.

such as ethanethiol (EtSH), shown in Fig. 1b. All samples possess the characteristic spin-orbit split A and B exciton peaks at ~ 1.9 eV and ~ 2.0 eV respectively. However, in the TFSI-treated sample, a subgap absorption feature appears around 1.7 eV. The experimentally measured absorption compares well to our computed GW-BSE absorbance, shown in Fig. 1a, bottom. The absorbance was calculated for a freestanding MoS₂ monolayer with a uniform 2 % concentration of sulfur vacancies, and for the same system but with an oxygen substitution at the defect site. As shown previously, the sulfur vacancies give rise to a subgap feature (X_{D2}), arising from electron-hole transitions between the defect states.¹⁸ The computed excitation energy associated with these transitions is in good agreement with the subgap features observed in experiment. In stark contrast, the calculated absorbance of the oxygen substitution system does not show any subgap states. This comparison to theory suggests that, surprisingly, the TFSI treatment opens up sulfur vacancy (SV) sites.

Fig. 1c presents a schematic overview of the quasiparticle bands associated with various defect configurations near the K and K' valleys in monolayer MoS₂. The sulfur vacancy introduces an occupied defect state close to the valence band edge and an unoccupied defect state deep in the bandgap.^{18,54} As we show below, these unoccupied states act as traps for excitons. According to our calculations, oxygen substitutions, which previously were shown to remove the subgap defect states,^{16,26,34} also do not introduce subgap features in the optical absorption spectrum. A possible route by which the TFSI can open up the sulfur vacancy defect site, as demonstrated schematically in Fig. 1c, is by removing substituted oxygen atoms from the untreated sample. Alternatively, charges from the dopants might shift the Fermi level, occupying the subgap defect states and rendering them inaccessible to optical excitations. The reduction in n -doping *via* the TFSI treatment (consistent with previous results and field-effect transistor (FET) measurements shown below) would then make these sites accessible.

In agreement with prior studies, we observe a large enhancement in PL for TFSI-treated samples, as shown in Fig. 2. The linewidth narrows by ~ 0.06 eV and the peak emission energy

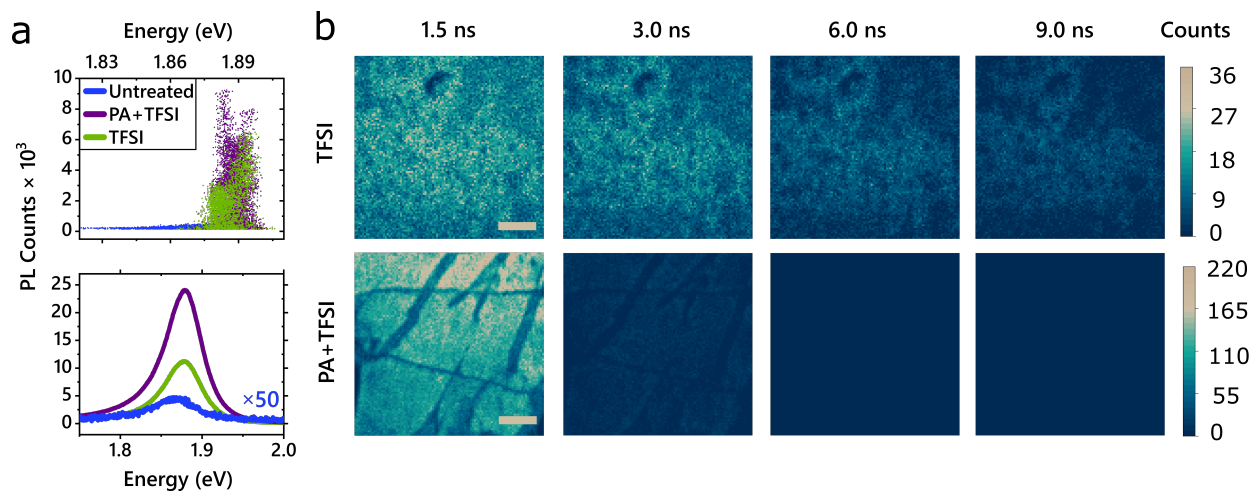


Figure 2: PL dynamics. a) Top: Energy (x-axis) *versus* maximum PL count (y-axis) for samples of each treatment condition, where each point represents a pixel of a PL map. TFSI and PA+TFSI treatments result in a blueshift and narrowing of the peak emission energy distribution. Mean and standard deviation are shown in Supplementary Information, Table 1. Bottom: Sample PL spectra illustrating the brightest spot measured under each treatment condition. With optimization, the PA+TFSI chemical treatment enhances the PL about twice as much as TFSI alone. b) PL maps illustrating the PL magnitude and intensity as a function of time after excitation, for TFSI-treated samples (top) and PA+TFSI treated samples (bottom). Scale bar corresponds to $4 \mu\text{m}$. Emission of untreated samples was instrument-response limited and thus shorter than 100 ps (see Supporting Information, Section 7).

blueshifts, as shown in Fig. 2a (and further statistics and data shown in the Supporting Information, Section 1). Representative measurements of the PL emission lineshape and intensity are shown in Fig. 2a, bottom. In Fig. 2b, we measured the PL intensity as a function of time and space for TFSI (top) and PA+TFSI (bottom) treated flakes. The PL emission lifetime for TFSI-treated samples is ~ 3.5 ns, with a standard deviation of 1.5 ns. The distribution of the average PL lifetime is between 1-20 ns, much longer than the PL lifetime of untreated MoS₂,^{55,56} which falls below the instrument response of 100 ps (See Supporting Information, Section 7). The observed longer PL lifetime upon TFSI treatment is consistent with previous results and has been suggested to arise due to a trap-mediated exciton recombination process following TFSI treatment.^{45,57} We note that in the absence of defects, shorter radiative exciton lifetimes are expected (based on their high absorption coefficients), allowing emission to outcompete non-radiative decay channels.⁵⁵

To further study the energy-resolved time evolution of the excited state in MoS₂, we performed ultrafast pump-probe measurements on monolayer flakes >150 μm in diameter (measurements were performed on multiple samples to ensure reproducibility, see Experimental Section). In these measurements, samples are excited with a narrowband, close-to-resonant pump pulse at 1.92 eV, and probed using a broadband white-light pulse. As shown in Fig. 3, both the untreated and TFSI-treated samples possess positive features around 2.03 eV and 1.88 eV. As the change in transmission is proportional to the change in the density of states, we assign these positive features to the bleach of the A and B excitons. When the A and B exciton states are populated, fewer photons are absorbed from the probe pulse, resulting in a positive signal in the differential pump-probe measurement.⁵⁸

In the TFSI-treated sample, Fig. 3a, middle, a positive feature in the near-IR appears at the same energy as the state previously observed in the steady-state absorption measurements (Fig. 1a,top). We attribute this feature to a bleach of the subgap defect state. This defect state is lower in energy and delocalized in momentum space, so excitons could be expected to funnel into these states. Indeed, we observe that the bleach of the A exciton in the

TFSI treated sample decays more significantly than the bleach of the untreated A exciton in the first 50 picoseconds (Fig. 3a, middle, inset, and Supporting information Section 2). Simultaneous with the initial A exciton decay (light green) is a growth of the subgap defect bleach (dark green), confirming a transfer in population from the band edge A excitons to the defect states. As the photoexcited excitons localize in these low-energy states, absorption into those states is reduced, thereby increasing the bleach signal. The hybridization of states is further corroborated by pump-probe measurements with pump energies resonant with the defect states (see Supporting Information, Section 4). While TFSI-treated samples show clear bleach signatures from the A and B excitons from time zero, untreated samples exhibit negligible signal for all times, illustrating that the untreated samples do not absorb the lower energy pump.

When excited above the bandgap, the emission from TFSI-treated samples is dominated by photons near the optical band edge, as shown in Fig. 3b, dark green. Surprisingly, with subgap excitation, resonant with the defect-state absorption at 1.70 eV, we also observe emission from the band edge at 1.88 eV (Fig. 3b, light green). Although the pump-probe measurements illustrate that carriers populate the subgap state, the emission does not occur at this energy. This is consistent with previous reports of temperature-dependent PL, suggesting that thermally-activated upconversion from trap states in TFSI-treated MoS₂ may be responsible for the enhanced PL.⁴⁵ Interestingly, based on our observations, upconversion from the defect state to the A exciton state must happen on faster timescales than the radiative and non-radiative decay of the defect exciton, for which previous works have measured long emission lifetimes.^{45,59,60} As discussed in the Supporting Information Section 8, we estimate, based on the Raman modes of the system, that thermal repopulation of the A exciton is possible on a timescale of hundreds of picoseconds to a nanosecond. This gives us a lower-bound on the defect exciton radiative and non-radiative decay rates, as both must be slower than the repopulation to the A exciton.

Thus we find that, at room temperature, TFSI treatment enhances emission, rather than

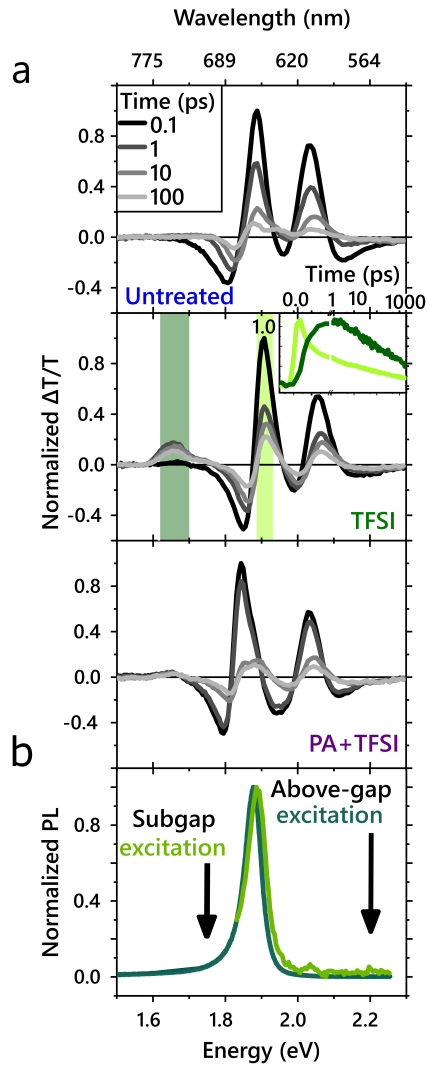


Figure 3: a) Pump-probe measurements of MoS₂ monolayers with different chemical treatments. Pump-probe spectra of MoS₂ untreated (top), TFSI-treated (middle), and PA+TFSI treated (bottom) MoS₂. TFSI treatment results in a prominent subgap bleach associated with sulfur vacancy defects. The inset shows the normalized kinetics taken at the A exciton bleach (light green) and defect peak (dark green) in the TFSI-treated sample, illustrating transfer from the band edge to the subgap defect state. b) PL emitted with subgap excitation of TFSI-treated MoS₂ occurs at the same energy as PL emitted by above-bandgap excitation of TFSI-treated MoS₂.

decreasing it. Emission occurs in spite of the presence of sulfur-vacancy-related subgap states, which trap excitons and prolong the PL lifetime. If these decay routes were faster than the repopulation of the A exciton, emission from the A exciton would be quenched as this defect-decay route would be the dominant process. At room temperature, there is sufficient energy to thermalize to the band edge, where excitons emit. Because the emission comes primarily from the neutral exciton, the linewidth narrows and blueshifts with respect to untreated samples where trion emission may lead to broadening.⁶¹ However, despite the increase in PL emission, we observed a decrease in free-carrier mobility by over two orders of magnitude in TFSI-treated FETs as compared to untreated FETs, shown in Fig. 4a. So while TFSI may increase PLQY, the SVs still trap carriers and play a significant role in the dynamics citeyu2014towards. This implies that the defects remain a barrier and significantly limit the quality of devices. Therefore, we seek to determine routes to passivate defects, as discussed below.

We aim to understand the passivation mechanism in order to rationally design chemical protocols to control defect nature and dynamics. Recent theoretical predictions suggest that a thiol bound to the SV in MoS₂ would push the site energy above the bandgap, hence effectively passivating the SV.^{62,63} Previous studies attempting to use thiol groups to passivate SVs in TMDCs have found them to be ineffective, resulting in a reduction in PL.⁶⁴ We speculate that this is because thiols are a minor *n*-dopant.^{65,66} When applied to MoS₂, though they may passivate defects, they add additional carriers and reduce the spectral weight of the neutral exciton, which limits the quantum yield.⁶¹ We therefore treat samples with a combination of a passivating agent (PA), which we show below can be from a range of different chemicals, and a strong Lewis acid, TFSI (Fig. 4b, top, Supporting information, Section 6).

The maximum PL spectra observed on a PA+TFSI treated sample is ~ 275 times brighter than the brightest point on untreated samples (Fig. 2a, bottom). The PL enhancement obtained by the two-step treatment is on average twice as large as for the TFSI-only treatment,

as shown in Fig. 2a, with further figures and statistics reported in the Supporting Information, Section 1. Similar to the TFSI-treated samples, the peak PL position blueshifts by roughly 30 meV, consistent with a decrease in trions. We illustrate the increased PL intensity and shortened emission lifetime through color maps, plotting the PL counts at different times after excitation, shown in Fig. 2b, bottom. The PL is both more intense and shorter in lifetime for the PA+TFSI sample than the TFSI-only sample. Further statistics comparing multiple flakes of each treatment condition are found in the Supporting Information, Section 1. The lifetime has a mean of 2.5 ns with a standard deviation of 1 ns (Supporting Information Table 2), shorter than the mean lifetime of TFSI-treated flakes, of 3.5 ns. Theoretical predictions of the PL lifetime for MoS₂ at room temperature are in the 500 ps to few-nanosecond time range.^{55,56} Thus, the lower lifetimes obtained *via* the two-step treatment are more in line with what would be expected from the intrinsic, non-trap limited PL decay. Turning to the steady-state absorption (Fig. 1a, top), no subgap states are observed for the two-step treatment, in contrast to the TFSI treatment. Correspondingly, in our pump-probe measurements (Fig. 3a, bottom), we observe a greatly reduced subgap bleach, which as discussed above arises from the subgap SV sites. This suggests that the two-step treatment greatly passivates these SV sites, while increasing PLQY above that achieved *via* TFSI-only treatment. Further optimization on these treatments should allow for complete passivation of the SV sites, resulting in higher PL yield and shorter, more intrinsic lifetimes.

The reduction in defect-trap-limited dynamics is further illustrated by FET measurements, establishing the free carrier mobility for each treatment condition. The field-effect mobility of TFSI-treated samples decreased by two orders of magnitude upon treatment (Fig. 4a, top). This could be partially due to a decrease in doping, as seen also in the threshold voltage shift (Fig. 4a, bottom). However, PA+TFSI treated samples exhibit field-effect mobilities of the same order of magnitude as untreated devices, despite a threshold voltage change comparable to TFSI-treated samples. When the carrier density is comparable to the charge trap density, a significant proportion of the carriers are localised, deteriorating the

charge carrier mobility.²⁵ As such, experimental reports typically observe mobility in MoS₂ increasing with increasing carrier density. The reduced field effect mobility we observe in TFSI is therefore expected due to the decreased carrier density, determined from a positive threshold voltage shift, approaching the charge trap density. In contrast, devices with PA + TFSI treatment exhibit a comparable positive threshold voltage shift but without a significant reduction in field effect mobility, indicating a reduction in the charge trap density relative to TFSI treatment alone. We therefore attribute this decrease in mobility in TFSI-treated MoS₂ to the prevalence of subgap SV sites, which can be greatly passivated by the two-step treatment developed here, thereby increasing mobilities in PA+TFSI treated samples relative to TFSI treatment alone.

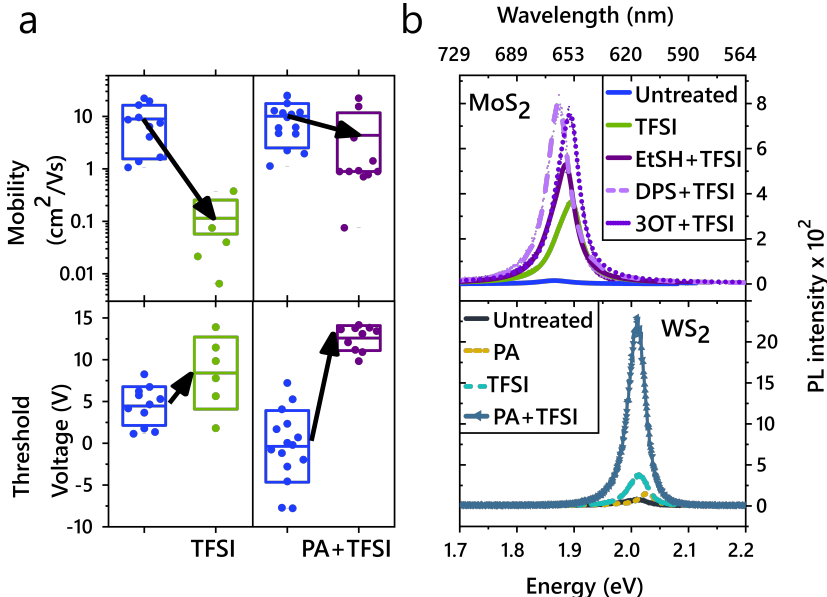


Figure 4: Device properties and generalizability of chemical treatment. a) Field-effect mobility (top) and threshold voltage shift (bottom) for FET devices before and after treatment, plotting the mean (solid line) and standard deviation (box) of measurements on different devices. Although both TFSI and PA+TFSI treatment decrease the threshold voltage, the PA+TFSI treatment maintains the mobility, whereas TFSI alone results in a significant reduction in mobility. b) Top: PL enhancement of MoS₂ using the different passivating agents outlined in Fig. 1b. Bottom: PL enhancement of various chemical treatments on WS₂. PA alone results in a very minimal increase in PL (also see Supporting Information Section 6).

We conclude by discussing the generalizability of the treatment methods presented in this work. First, in Fig. 4b, top, we show that the initial passivation step is achievable

using a range of chemicals with sulfur in the -2 oxidation state, such as sulfides and thiols. Second, to confirm that our results can be generalized to other sulfur-based TMDCs, we illustrate similar PL enhancements on WS₂ shown in Fig. 4b, bottom. Thus, guided by the understanding of defects in these materials, we are able to design a passivation protocol for reducing SV defects. We illustrate that PLQY alone is insufficient to determine material quality in 2D materials, as PL can significantly increase even in the presence of sulfur vacancy defects. Our study of the absorption and PL lifetime upon different chemical treatments in MoS₂ and WS₂ highlights the importance of designing mechanistic chemical treatments to reduce the influence of defects and increase the material functionality.

Conclusions

These protocols, however, are not limited solely to passivation of defects. Instead, we identify a treatment scheme for defect engineering of TMDCs. By tuning material properties *via* a simple, solution-based method, such rational passivation strategies can allow for defects to be used as a handle, rather than a hindrance. Along with improvements in properties like PL and mobility, we identify a possible design rule for effective treatments, and a wider range of chemicals with -2 sulfur as an effective defect engineering route for specific functionality or to break a symmetry,⁶⁷ which is beyond the scope of this work. These chemical passivation routes can also be easily translated into device manufacturing, allowing for both improved devices and device capabilities.

Experimental section

Sample preparation

Samples are exfoliated from bulk MoS₂ and WS₂ from 2DSemiconductors following the gold-evaporation method previously reported,⁵³ onto either quartz or Si/SiO₂ substrates. Further information on their sample quality is shown in the Supporting Information, Section 3.

Chemicals

All solvents used in chemical treatments were anhydrous and purchased from Sigma Aldrich. 3-n-octylthiophene was purchased from Tokyo Chemical Industry UK LTD and used directly. Other chemicals used in these treatments were purchased from Sigma Aldrich and used as received.

TFSI preparation and treatment

Three different concentrations of TFSI solutions were used in this work. 0.02 mg/mL and 2 mg/mL TFSI solutions were prepared according to the literature.⁴ 5 mg/mL (~0.018 M) TFSI solution was prepared in a nitrogen glovebox by dissolving 100 mg TFSI in 20 mL 1, 2-dichlorethane (DCE). The PL intensity of TFSI-treated MoS₂ and WS₂ increased while increasing the concentration of TFSI, until 5 mg/mL after which it saturated. Samples are submerged in TFSI solution for ~30 min then dried with a nitrogen gun. The TFSI solution could also be drop casted. We found no significant difference between these two methods. All the preparation of chemical solutions and chemical treatments were carried out in a nitrogen glovebox.

Ethanethiol preparation and treatment

The 0.1 M ethanethiol solution was prepared by mixing 14.8 μL ethanethiol with 20 mL acetonitrile. 0.1 M ethanethiol/acetonitrile was spin coated on the TMDC sample at 1000 rpm for 1 min. The sample was rinsed in toluene to remove extra ethanethiol which was not chemisorbed on the TMDC surface and was dried with a N_2 gun. Finally, the sample was placed on a hotplate at 100 $^\circ\text{C}$ for 5 min. We found that the annealing step had no impact on optical and electronic properties of samples and was used to decrease the drying time. The ethanethiol was also compatible with dichloromethane and 1,2-dichloroethane.

Dipropyl sulfide and 3-n-octylthiophene preparation and treatment

The 0.1 M dipropyl sulfide solution was prepared by mixing 282 μL dipropyl sulfide with 20 mL dichloromethane. The 0.1 M 3-n-octylthiophene solution was prepared by mixing 427 μL 3-n-octylthiophene with 20 mL dichloromethane. Samples were submerged in 4 mL chemical solutions in a 25 mL glass vial overnight after which the samples were rinsed in dichloromethane and dried with a nitrogen gun.

Absorption

Steady-state absorption measurements are performed in transmission on a Zeiss Axiovert inverted microscope with a halogen white light source and a Zeiss EC Epiplan Apochromat 50 \times objective (numerical aperture (NA) = 0.95). The light transmitted through the sample is coupled to a UV600 nm optical fiber connected to a spectrometer (AvaspecHS2048, Avantes).

Steady-state PL measurements

Multiple experimental setups were used to measure photoluminescence, however data that is displayed on the same figure is always measured on the same setup under the same conditions.

In a WITec Alpha 300 s setup,⁶⁸ a 405 nm continuous wave laser (Coherent CUBE) is

fibre coupled into a microscope with a 20x Olympus lens to excite the sample. The emitted PL is collected through the same 20x objective then sent to a Princeton Instruments SP-2300i spectrometer and an Andor iDus 401 CCD detector. All PL is measured at 30 Wcm^{-2} . Data from this setup is shown in Fig. 4b, bottom and Supporting information, Section 1.

A second setup is used for measurements where untreated MoS_2 is directly compared to chemically treated samples (Fig. 2a, Supporting Information Section 6), and Fig. 4b, top). This is performed on a Renishaw Invia confocal setup, excited with a 514.5 Ar-ion continuous wave laser, exciting with a 20x objective and $\sim 30 \text{ Wcm}^{-2}$. The PL is collected in reflection and dispersed using a 600 L/mm grating onto a CCD detector.

The upconversion PL measurement (Fig. 3b) is performed on a home-built linear PL setup. For above-bandgap excitation, we use a 405 nm laser (Coherent Obis 405) exciting with $\sim 52 \text{ mWcm}^{-2}$. For subgap excitation, we excite with a 730 nm diode laser (Thorlabs) with $\sim 2 \text{ Wcm}^{-2}$. PL is collected with a lens and focused into an Andor Kymera 328i Spectrometer, and then recorded with a Si-CCD (Andor iDus 420). In the subgap excitation measurement, a shortpass filter at 700 nm is used to remove the laser, though a small tail is still observed.

Further PL measurements in the supporting information, Section 3, is carried out on a Renishaw inVia Raman confocal microscope with a 532 nm excitation laser in air under ambient condition. The Raman emission was collected by a $50\times$ long working distance objective lens in streamline mode and dispersed by a 1800 l/mm grating with 1% of the laser power ($< 10 \mu\text{W}$). The spectrometer was calibrated to a silicon reference sample prior to the measurement to correct for the instrument response

Time-resolved PL measurements

Time-resolved measurements are performed using a PicoQuant Microtime 200 confocal time-resolved PL setup. Samples are excited with a 405 nm, 20 MHz pulsed laser focused by a 20x objective (0.6 Numerical Aperture), and emitted PL is collected in reflection mode, and

sent to a hybrid photomultiplier tube (PMT) detector from Picoquant for single photon counting. The emission signal was separated from the excitation light (405 nm) using a dichroic mirror (Z405RDC, Chroma). On the emission path, a pinhole (50 μm) is used for the spatial filtering, as well as an additional 410 nm longpass filter. Repetition rates of 27 MHz were used for the maps. The instrument response is measured to be ~ 100 ps (Supporting Information Section 7). 100 nW of power is used to excite a $\sim 2.5 \times 2.5 \mu\text{m}^2$ area, corresponding to a 80 nJcm^{-2} fluence. At each point, the PL intensity, and time-resolved photoluminescence decay curve is measured. The PL counts are binned into four time intervals, 0-1.5 ns, 1.5-3 ns, 3-6 ns, and 6-9 ns. This binning of data is then plotted in Fig. 2b. Every spatial datapoint can also be thought of as a distribution of photons arriving at different delays after the excitation pulse, also called photons delay histogram. This allows us to evaluate the PL lifetime, by measuring the weighted average of the photon histogram at each point. Both the PL intensity and the PL decays are plotted in a scatter plot shown in the Supporting information, Fig.1,bottom. Untreated samples have a short decay lifetime, < 100 ps, as the experimentally measured PL lifetime is instrument-response limited (Supporting Information Section 7). Finally, the statistics from these data are shown in Supporting Information, Table 1.

Pump-probe

Pump-probe measurements are performed using a Light Conversion Pharos, Yb-based system, with 400 μJ per pulse at 1030 nm and a repetition rate of 38 kHz. The output of the Pharos is split and sent along two paths, one to generate the pump, and the second the probe. In the pump path, the fundamental of the laser is sent into a narrow-band optical parametric oscillator system, (ORPHEUS-LYRA, Light Conversion), where ~ 250 fs FWHM pulses are generated, for most measurements in this work, at 500 nm. The pump is chopped with a mechanical chopper to generate an on-off pattern with respect to the probe pulse. The probe is generated by focusing the fundamental of the laser into a 4 mm YAG crystal,

producing a broadband probe from 520 nm to 950 nm. The probe is delayed with respect to the pump, using a computer controlled mechanical delay stage (Newport). The probe, of roughly $80 \times 80 \mu\text{m}^2$ in spot size, is kept intentionally smaller than the $\sim 250 \times 250 \mu\text{m}^2$ pump. The monolayer is found by centering a $\sim 200 \mu\text{m}^2$ diameter onto the substrate when under a microscope, then aligning the probe through the center of this pinhole. The detected probe is collected on a silicon line scan camera (AViiVA EM2/EM4) with a visible monochromator 550 nm blazed grating. Data shown for the untreated and PA+TFSI treatment are taken from the same sample (measured before and after treatment). This data is also representative of measurements taken over many samples for each treatment condition (>15 TFSI-treated samples, >15 untreated samples, and >5 PA+TFSI treated samples).

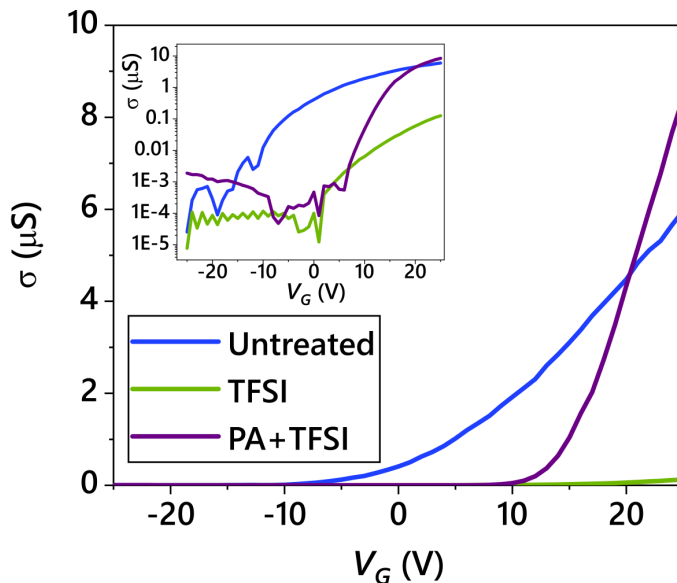


Figure 5: Sample transport characteristics. An example of the gate voltage *versus* mobility for different chemical treatment steps.

Device preparation and measurement

To determine the effects of the treatments on the electronic properties of the MoS_2 we fabricated field-effect transistors. MoS_2 was transferred onto Si with 90 nm of thermally

grown SiO₂, which acted as a global back gate. Monolayer MoS₂ flakes were identified and Au contacts made by electron beam lithography and thermal evaporation. The MoS₂ channels have a typical length of 5 μm from source to drain. Transfer characteristics were measured with a source-drain bias of $V_{DS}=1$ V using a Keithley 4200-SCS parameter analyzer and probe station under dark ambient conditions. Example transfer curves showing the conductivity $\sigma = \frac{L}{W} \frac{I_D}{V_{DS}}$ as a function of back gate V_G for MoS₂ devices after different treatments are plotted below in Fig. 5, where L and W are the length and width respectively, I_D is the measured current.

Associated content

This Supporting Information is available free of charge *via* the internet at <http://pubs.acs.org>.

This contains:

- Further data and statistical analysis of PL emission enhancement and PL lifetimes
- Data showing the untreated samples' PL lifetime and comparisons with the instrument response
- Pump-probe measurements of PA only treated samples
- Analysis of the kinetic lifetimes in pump-probe
- PL comparison of exfoliation methods
- Subgap pump-probe measurements
- Discussion and data on varying the treatment order
- Discussion and calculations using the Arrhenius equation
- Further descriptions of the GW-BSE theory calculation
- Discussion on substitutional oxygen and Fermi level

- References^{69–74}

This study is also associated with Ref.⁷⁵ on the preprint server, Arxiv.

Acknowledgments

We thank the Engineering and Physical Sciences Research Council (EPSRC) and the Winton Programme for the Physics of Sustainability for funding. J.A-W. acknowledges the support of his Research Fellowship from the Royal Commission for the Exhibition of 1851 and Royal Society Dorothy Hodgkin Research Fellowship. S.D.S acknowledges support from the Royal Society and Tata Group (UF150033). G.D. acknowledges the Royal Society for funding through a Newton International Fellowship. This project has received funding from the European Research Council (ERC) under the European Union’s Horizon 2020 research and innovation programme (Grant Agreements 758826 and 756962). Z.L. acknowledges funding from the Swedish research council, Vetenskapsrådet 2018-06610. This work was supported by the Center for Computational Study of Excited State Phenomena in Energy Materials, which is funded by the U.S. Department of Energy, Office of Science, Basic Energy Sciences, Materials Sciences and Engineering Division under Contract No. DE-AC02-05CH11231, as part of the Computational Materials Sciences Program. Work performed at the Molecular Foundry was also supported by the Office of Science, Office of Basic Energy Sciences, of the U.S. Department of Energy under the same contract number. S. R. A. acknowledges Rothschild and Fulbright fellowships. This research used resources of the National Energy Research Scientific Computing Center (NERSC), a DOE Office of Science User Facility supported by the Office of Science of the U.S. Department of Energy under Contract No. DE-AC02-05CH11231.

References

1. Mak, K. F.; Lee, C.; Hone, J.; Shan, J.; Heinz, T. F. Atomically Thin MoS₂: A New Direct-Gap Semiconductor. *Physical Review Letters* **2010**, *105*, 136805.
2. Splendiani, A.; Sun, L.; Zhang, Y.; Li, T.; Kim, J.; Chim, C.-Y.; Galli, G.; Wang, F. Emerging Photoluminescence in Monolayer MoS₂. *Nano Letters* **2010**, *10*, 1271–1275.
3. Chernikov, A.; Berkelbach, T. C.; Hill, H. M.; Rigosi, A.; Li, Y.; Aslan, Ö. B.; Reichman, D. R.; Hybertsen, M. S.; Heinz, T. F. Excitons in Atomically Thin Transition-Metal Dichalcogenides. 2014 Conference on Lasers and Electro-Optics (CLEO)-Laser Science to Photonic Applications. 2014; pp 1–2.
4. Amani, M.; Lien, D.-H.; Kiriya, D.; Xiao, J.; Azcatl, A.; Noh, J.; Madhupathy, S. R.; Addou, R.; Santosh, K.; Dubey, M.; Cho, K.; Wallace, R. M.; Lee, S.-C.; He, J.-H.; Ager III, J. W.; Zhang, X.; Yablonovitch, E.; Javey, A. Near-Unity Photoluminescence Quantum Yield in MoS₂. *Science* **2015**, *350*, 1065–1068.
5. Wang, H.; Zhang, C.; Rana, F. Ultrafast Dynamics of Defect-Assisted Electron–Hole Recombination in Monolayer MoS₂. *Nano Letters* **2015**, *15*, 339–345.
6. Yuan, S.; Roldán, R.; Katsnelson, M.; Guinea, F. Effect of Point Defects on the Optical and Transport Properties of MoS₂ and WS₂. *Physical Review B* **2014**, *90*, 041402.
7. Wang, G.; Chernikov, A.; Glazov, M. M.; Heinz, T. F.; Marie, X.; Amand, T.; Urbaszek, B. Colloquium: Excitons in Atomically Thin Transition Metal Dichalcogenides. *Reviews of Modern Physics* **2018**, *90*, 021001.
8. Kang, N.; Paudel, H. P.; Leuenberger, M. N.; Tetard, L.; Khondaker, S. I. Photoluminescence Quenching in Single-Layer MoS₂ via Oxygen Plasma Treatment. *The Journal of Physical Chemistry C* **2014**, *118*, 21258–21263.

9. Rhodes, D.; Chae, S. H.; Ribeiro-Palau, R.; Hone, J. Disorder in van der Waals Heterostructures of 2D Materials. *Nature materials* **2019**, *18*, 541.
10. Qiu, H.; Xu, T.; Wang, Z.; Ren, W.; Nan, H.; Ni, Z.; Chen, Q.; Yuan, S.; Miao, F.; Song, F.; Long, G.; Shi, Y.; Sun, L.; Wang, J.; Wang, X. Hopping Transport through Defect-Induced Localized States in Molybdenum Disulphide. *Nature communications* **2013**, *4*, 1–6.
11. Ghatak, S.; Pal, A. N.; Ghosh, A. Nature of Electronic States in Atomically Thin MoS₂ Field-Effect Transistors. *ACS Nano* **2011**, *5*, 7707–7712.
12. Schmidt, H.; Giustiniano, F.; Eda, G. Electronic Transport Properties of Transition Metal Dichalcogenide Field-Effect Devices: Surface and Interface Effects. *Chemical Society Reviews* **2015**, *44*, 7715–7736.
13. Wu, Z.; Ni, Z. Spectroscopic Investigation of Defects in Two-Dimensional Materials. *Nanophotonics* **2017**, *6*, 1219–1237.
14. Tian, X.; Kim, D. S.; Yang, S.; Ciccarino, C. J.; Gong, Y.; Yang, Y.; Yang, Y.; Duschatko, B.; Yuan, Y.; Ajayan, P. M.; Idrobo, J. C.; Narang, P.; Miao, J. Correlating the Three-Dimensional Atomic Defects and Electronic Properties of Two-Dimensional Transition Metal Dichalcogenides. *Nature Materials* **2020**, 1–7.
15. Aghajanian, M.; Schuler, B.; Cochrane, K. A.; Lee, J.-H.; Kastl, C.; Neaton, J. B.; Weber-Bargioni, A.; Mostofi, A. A.; Lischner, J. Resonant and Bound States of Charged Defects in Two-Dimensional Semiconductors. *Physical Review B* **2020**, *101*, 081201.
16. Barja, S.; Refaely-Abramson, S.; Schuler, B.; Qiu, D. Y.; Pulkin, A.; Wickenburg, S.; Ryu, H.; Ugeda, M. M.; Kastl, C.; Chen, C.; Hwang, C.; Schwartzberg, A.; Aloni, S.; Mo, S.-K.; Ogletree, D. F.; Crommie, M. F.; Yazyev, O. V.; Louie, S. G.; Neaton, J. B.; Weber-Bargioni, A. Identifying Substitutional Oxygen as a Prolific Point Defect in Monolayer Transition Metal Dichalcogenides. *Nature communications* **2019**, *10*, 1–8.

17. Schuler, B.; Qiu, D. Y.; Refaely-Abramson, S.; Kastl, C.; Chen, C. T.; Barja, S.; Koch, R. J.; Ogletree, D. F.; Aloni, S.; Schwartzberg, A. M.; Neaton, J. B.; Louie, S. G.; Weber-Bargioni, A. Large Spin-Orbit Splitting of Deep In-Gap Defect States of Engineered Sulfur Vacancies in Monolayer WS₂. *Physical Review Letters* **2019**, *123*, 076801.
18. Refaely-Abramson, S.; Qiu, D. Y.; Louie, S. G.; Neaton, J. B. Defect-Induced Modification of Low-Lying Excitons and Valley Selectivity in Monolayer Transition Metal Dichalcogenides. *Physical Review Letters* **2018**, *121*, 167402.
19. Lin, Z.; Carvalho, B. R.; Kahn, E.; Lv, R.; Rao, R.; Terrones, H.; Pimenta, M. A.; Terrones, M. Defect Engineering of Two-Dimensional Transition Metal Dichalcogenides. *2D Materials* **2016**, *3*, 022002.
20. Zhou, W.; Zou, X.; Najmaei, S.; Liu, Z.; Shi, Y.; Kong, J.; Lou, J.; Ajayan, P. M.; Yakobson, B. I.; Idrobo, J.-C. Intrinsic Structural Defects in Monolayer Molybdenum Disulfide. *Nano Letters* **2013**, *13*, 2615–2622.
21. Haldar, S.; Vovusha, H.; Yadav, M. K.; Eriksson, O.; Sanyal, B. Systematic Study of Structural, Electronic, and Optical Properties of Atomic-Scale Defects in the Two-Dimensional Transition Metal Dichalcogenides MX₂ (M= Mo, W; X= S, Se, Te). *Physical Review B* **2015**, *92*, 235408.
22. Komsa, H.-P.; Kotakoski, J.; Kurasch, S.; Lehtinen, O.; Kaiser, U.; Krasheninnikov, A. V. Two-Dimensional Transition Metal Dichalcogenides under Electron Irradiation: Defect Production and Doping. *Physical Review Letters* **2012**, *109*, 035503.
23. Hong, J.; Hu, Z.; Probert, M.; Li, K.; Lv, D.; Yang, X.; Gu, L.; Mao, N.; Feng, Q.; Xie, L.; Zhang, J.; Wu, D.; Zhang, Z.; Jin, C.; Ji, W.; Zhang, X.; Yuan, J.; Zhang, Z. Exploring Atomic Defects in Molybdenum Disulphide Monolayers. *Nature communications* **2015**, *6*, 1–8.

24. Liu, D.; Guo, Y.; Fang, L.; Robertson, J. Sulfur Vacancies in Monolayer MoS₂ and Its Electrical Contacts. *Applied Physics Letters* **2013**, *103*, 183113.
25. Yu, Z.; Pan, Y.; Shen, Y.; Wang, Z.; Ong, Z.-Y.; Xu, T.; Xin, R.; Pan, L.; Wang, B.; Sun, L.; Wang, J.; Zhang, G.; Zhang, Y. W.; Shi, Y.; Wang, X. Towards Intrinsic Charge Transport in Monolayer Molybdenum Disulfide by Defect and Interface Engineering. *Nature communications* **2014**, *5*, 1–7.
26. Pető, J.; Ollár, T.; Vancsó, P.; Popov, Z. I.; Magda, G. Z.; Dobrik, G.; Hwang, C.; Sorokin, P. B.; Tapasztó, L. Spontaneous Doping of the Basal Plane of MoS₂ Single Layers through Oxygen Substitution under Ambient Conditions. *Nature chemistry* **2018**, *10*, 1246–1251.
27. Li, H.; Tsai, C.; Koh, A. L.; Cai, L.; Contryman, A. W.; Fragapane, A. H.; Zhao, J.; Han, H. S.; Manoharan, H. C.; Abild-Pedersen, F.; Nørskov, J. K.; Zheng, X. Activating and Optimizing MoS₂ Basal Planes for Hydrogen Evolution through the Formation of Strained Sulphur Vacancies. *Nature materials* **2016**, *15*, 48–53.
28. Lu, H.; Kummel, A.; Robertson, J. Passivating the Sulfur Vacancy in Monolayer MoS₂. *APL Materials* **2018**, *6*, 066104.
29. Mouri, S.; Miyauchi, Y.; Matsuda, K. Tunable Photoluminescence of Monolayer MoS₂ via Chemical Doping. *Nano Letters* **2013**, *13*, 5944–5948.
30. Han, H.-V.; Lu, A.-Y.; Lu, L.-S.; Huang, J.-K.; Li, H.; Hsu, C.-L.; Lin, Y.-C.; Chiu, M.-H.; Suenaga, K.; Chu, C.-W.; Kuo, H.-C.; Chang, W.-H.; Li, L.-J.; Shi, Y. Photoluminescence Enhancement and Structure Repairing of Monolayer MoSe₂ by Hydrohalic Acid Treatment. *ACS Nano* **2016**, *10*, 1454–1461.
31. Kim, Y.; Lee, Y.; Kim, H.; Roy, S.; Kim, J. Near-Field Exciton Imaging of Chemically Treated MoS₂ Monolayers. *Nanoscale* **2018**, *10*, 8851–8858.

32. Atallah, T.; Wang, J.; Bosch, M.; Seo, D.; Burke, R.; Moneer, O.; Zhu, J.; Theibault, M.; Brus, L.; Hone, J.; Zhu, X.-Y. Electrostatic Screening of Charged Defects in Monolayer MoS₂. *The journal of physical chemistry letters* **2017**, *8*, 2148–2152.
33. Zhang, S.; Hill, H. M.; Moudgil, K.; Richter, C. A.; Hight Walker, A. R.; Barlow, S.; Marder, S. R.; Hacker, C. A.; Pookpanratana, S. J. Controllable, Wide-Ranging *n*-Doping and *p*-Doping of Monolayer Group 6 Transition-Metal Disulfides and Diselenides. *Advanced Materials* **2018**, *30*, 1802991.
34. Nan, H.; Wang, Z.; Wang, W.; Liang, Z.; Lu, Y.; Chen, Q.; He, D.; Tan, P.; Miao, F.; Wang, X.; Wang, J.; Ni, Z. Strong Photoluminescence Enhancement of MoS₂ through Defect Engineering and Oxygen Bonding. *ACS Nano* **2014**, *8*, 5738–5745.
35. Tongay, S.; Zhou, J.; Ataca, C.; Liu, J.; Kang, J. S.; Matthews, T. S.; You, L.; Li, J.; Grossman, J. C.; Wu, J. Broad-Range Modulation of Light Emission in Two-Dimensional Semiconductors by Molecular Physisorption Gating. *Nano Letters* **2013**, *13*, 2831–2836.
36. Ahn, H.; Huang, Y.-C.; Lin, C.-W.; Chiu, Y.-L.; Lin, E.-C.; Lai, Y.-Y.; Lee, Y.-H. Efficient Defect Healing of Transition Metal Dichalcogenides by Metallophthalocyanine. *ACS applied materials & interfaces* **2018**, *10*, 29145–29152.
37. Yao, H.; Liu, L.; Wang, Z.; Li, H.; Chen, L.; Pam, M. E.; Chen, W.; Yang, H. Y.; Zhang, W.; Shi, Y. Significant Photoluminescence Enhancement in WS₂ Monolayers through Na₂S Treatment. *Nanoscale* **2018**, *10*, 6105–6112.
38. Peimyoo, N.; Yang, W.; Shang, J.; Shen, X.; Wang, Y.; Yu, T. Chemically Driven Tunable Light Emission of Charged and Neutral Excitons in Monolayer WS₂. *ACS Nano* **2014**, *8*, 11320–11329.
39. Lien, D.-H.; Uddin, S. Z.; Yeh, M.; Amani, M.; Kim, H.; Ager, J. W.; Yablonovitch, E.; Javey, A. Electrical Suppression of All Nonradiative Recombination Pathways in Monolayer Semiconductors. *Science* **2019**, *364*, 468–471.

40. Chiu, M.-H.; Zhang, C.; Shiu, H.-W.; Chuu, C.-P.; Chen, C.-H.; Chang, C.-Y. S.; Chen, C.-H.; Chou, M.-Y.; Shih, C.-K.; Li, L.-J. Determination of Band Alignment in the Single-Layer MoS₂/WSe₂ Heterojunction. *Nature communications* **2015**, *6*, 1–6.
41. McDonnell, S.; Addou, R.; Buie, C.; Wallace, R. M.; Hinkle, C. L. Defect-Dominated Doping and Contact Resistance in MoS₂. *ACS Nano* **2014**, *8*, 2880–2888.
42. Bruix, A.; Miwa, J. A.; Hauptmann, N.; Wegner, D.; Ulstrup, S.; Grønborg, S. S.; Sanders, C. E.; Dendzik, M.; Čabo, A. G.; Bianchi, M.; Lauritsen, A. A., Jeppe V. and Khajetoorians; Hammer, B.; Hofmann, P. Single-Layer MoS₂ on Au (111): Band Gap Renormalization and Substrate Interaction. *Physical Review B* **2016**, *93*, 165422.
43. Zhou, Y.; Scuri, G.; Wild, D. S.; High, A. A.; Dibos, A.; Jauregui, L. A.; Shu, C.; De Greve, K.; Pistunova, K.; Joe, A. Y.; Taniguchi, T.; Watanabe, K.; Kim, P.; Lukin, M. D.; Park, H. Probing Dark Excitons in Atomically Thin Semiconductors *via* Near-Field Coupling to Surface Plasmon Polaritons. *Nature nanotechnology* **2017**, *12*, 856.
44. Kulig, M.; Zipfel, J.; Nagler, P.; Blanter, S.; Schüller, C.; Korn, T.; Paradiso, N.; Glazov, M. M.; Chernikov, A. Exciton Diffusion and Halo Effects in Monolayer Semiconductors. *Physical Review Letters* **2018**, *120*, 207401.
45. Goodman, A. J.; Willard, A. P.; Tisdale, W. A. Exciton Trapping is Responsible for the Long Apparent lifetime in Acid-Treated MoS₂. *Physical Review B* **2017**, *96*, 121404.
46. Amani, M.; Taheri, P.; Addou, R.; Ahn, G. H.; Kiriya, D.; Lien, D.-H.; Ager III, J. W.; Wallace, R. M.; Javey, A. Recombination Kinetics and Effects of Superacid Treatment in Sulfur-and Selenium-Based Transition Metal Dichalcogenides. *Nano Letters* **2016**, *16*, 2786–2791.
47. Tanoh, A. O. A.; Alexander-Webber, J.; Xiao, J.; Delport, G.; Williams, C. A.; Bretscher, H.; Gauriot, N.; Allardice, J.; Pandya, R.; Fan, Y.; Li, Z.; Vignolini, S.;

- Stranks, S. D.; Hofmann, S.; Rao, A. Enhancing Photoluminescence and Mobilities in WS₂ Monolayers with Oleic Acid Ligands. *Nano Letters* **2019**, *19*, 6299–6307.
48. Hybertsen, M. S.; Louie, S. G. Electron Correlation in Semiconductors and Insulators: Band Gaps and Quasiparticle Energies. *Physical Review B* **1983**, *34*, 5390–5413.
49. Hybertsen, M. S.; Louie, S. G. First-Principles Theory of Quasiparticles: Calculation of Band Gaps in Semiconductors and Insulators. *Physical Review Letters* **1985**, *55*, 1418.
50. Rohlfing, M.; Louie, S. G. Electron-Hole Excitations in Semiconductors and Insulators. *Physical Review Letters* **1998**, *81*, 2312.
51. Rohlfing, M.; Louie, S. G. Electron-Hole Excitations and Optical Spectra from First Principles. *Physical Review B* **2000**, *62*, 4927.
52. Momma, K.; Izumi, F. VESTA 3 for Three-Dimensional Visualization of Crystal, Volumetric and Morphology Data. *Journal of Applied Crystallography* **2011**, *44*, 1272–1276.
53. Desai, S. B.; Madhvapathy, S. R.; Amani, M.; Kiriya, D.; Hettick, M.; Tosun, M.; Zhou, Y.; Dubey, M.; Ager III, J. W.; Chrzan, D.; Javey, A. Gold-Mediated Exfoliation of Ultralarge Optoelectronically-Perfect Monolayers. *Advanced Materials* **2016**, *28*, 4053–4058.
54. Naik, M. H.; Jain, M. Substrate Screening Effects on the Quasiparticle Band Gap and Defect Charge Transition Levels in MoS₂. *Physical Review Materials* **2018**, *2*, 084002.
55. Palummo, M.; Bernardi, M.; Grossman, J. C. Exciton Radiative Lifetimes in Two-Dimensional Transition Metal Dichalcogenides. *Nano Letters* **2015**, *15*, 2794–2800.
56. Korn, T.; Heydrich, S.; Hirmer, M.; Schmutzler, J.; Schüller, C. Low-Temperature Photocarrier Dynamics in Monolayer MoS₂. *Applied Physics Letters* **2011**, *99*, 102109.

57. Linhart, L.; Paur, M.; Smejkal, V.; Burgdörfer, J.; Mueller, T.; Libisch, F. Localized Intervalley Defect Excitons as Single-Photon Emitters in WSe₂. *Physical Review Letters* **2019**, *123*, 146401.
58. Pogna, E. A.; Marsili, M.; De Fazio, D.; Dal Conte, S.; Manzoni, C.; Sangalli, D.; Yoon, D.; Lombardo, A.; Ferrari, A. C.; Marini, A.; Cerullo, G.; Prezzi, D. Photo-Induced Bandgap Renormalization Governs the Ultrafast Response of Single-Layer MoS₂. *ACS Nano* **2016**, *10*, 1182–1188.
59. Moody, G.; Tran, K.; Lu, X.; Autry, T.; Fraser, J. M.; Mirin, R. P.; Yang, L.; Li, X.; Silverman, K. L. Microsecond Valley Lifetime of Defect-Bound Excitons in Monolayer WSe₂. *Physical Review Letters* **2018**, *121*, 057403.
60. Klein, J.; Lorke, M.; Florian, M.; Sigger, F.; Sigl, L.; Rey, S.; Wierzbowski, J.; Cerne, J.; Müller, K.; Mitterreiter, E.; Zimmermann, P.; Taniguchi, T.; Watanabe, K.; Wurstbauer, U.; Kaniber, M.; Knap, M.; Schmidt, R.; Finley, J.; Holleitner, A. Site-Selectively Generated Photon Emitters in Monolayer MoS₂ *via* Local Helium Ion Irradiation. *Nature Communications* **2019**, *10*, 1–8.
61. Mak, K. F.; He, K.; Lee, C.; Lee, G. H.; Hone, J.; Heinz, T. F.; Shan, J. Tightly Bound Trions in Monolayer MoS₂. *Nature materials* **2013**, *12*, 207–211.
62. Li, Q.; Zhao, Y.; Ling, C.; Yuan, S.; Chen, Q.; Wang, J. Towards a Comprehensive Understanding of the Reaction Mechanisms between Defective MoS₂ and Thiol Molecules. *Angewandte Chemie International Edition* **2017**, *56*, 10501–10505.
63. Foörster, A.; Gemming, S.; Seifert, G.; Tomašnek, D. Chemical and Electronic Repair Mechanism of Defects in MoS₂ Monolayers. *ACS Nano* **2017**, *11*, 9989–9996.
64. Cho, K.; Min, M.; Kim, T.-Y.; Jeong, H.; Pak, J.; Kim, J.-K.; Jang, J.; Yun, S. J.; Lee, Y. H.; Hong, W.-K.; Lee, T. Electrical and Optical Characterization of MoS₂ with

- Sulfur Vacancy Passivation by Treatment with Alkanethiol Molecules. *ACS Nano* **2015**, *9*, 8044–8053.
65. Ugeda, M. M.; Bradley, A. J.; Shi, S.-F.; Felipe, H.; Zhang, Y.; Qiu, D. Y.; Ruan, W.; Mo, S.-K.; Hussain, Z.; Shen, Z.-X.; Wang, F.; Louie, S. G.; Crommie, M. F. Giant Bandgap Renormalization and Excitonic Effects in a Monolayer Transition Metal Dichalcogenide Semiconductor. *Nature materials* **2014**, *13*, 1091–1095.
66. Choi, S.; Kwon, K. C.; Kim, S. Y.; Jang, H. W. Tailoring Catalytic Activities of Transition Metal Disulfides for Water Splitting. *FlatChem* **2017**, *4*, 68–80.
67. Du, L.; Hasan, T.; Castellanos-Gomez, A.; Liu, G.-B.; Yao, Y.; Lau, C. N.; Sun, Z. Engineering Symmetry Breaking in 2D Layered Materials. *Nature Reviews Physics* **2021**, 1–14.
68. Tainter, G. D.; Hörantner, M. T.; Pazos-Outón, L. M.; Lamboll, R. D.; Āboliņš, H.; Leijtens, T.; Mahesh, S.; Friend, R. H.; Snaith, H. J.; Joyce, H. J.; Deschler, F. Long-Range Charge Extraction in Back-Contact Perovskite Architectures *via* Suppressed Recombination. *Joule* **2019**, *3*, 1301–1313.
69. Lee, C.; Yan, H.; Brus, L. E.; Heinz, T. F.; Hone, J.; Ryu, S. Anomalous Lattice Vibrations of Single- and Few-Layer MoS₂. *ACS Nano* **2010**, *4*, 2695–2700.
70. Kohn, W.; Sham, L. J. Self-Consistent Equations Including Exchange and Correlation Effects. *Physical review* **1965**, *140*, A1133.
71. Giannozzi, P.; Baroni, S.; Bonini, N.; Calandra, M.; Car, R.; Cavazzoni, C.; Ceresoli, D.; Chiarotti, G. L.; Cococcioni, M.; Dabo, I.; Dal Corso, A.; de Gironcoli, S.; Fabris, S.; Fratesi, G.; Gebauer, R.; Gerstmann, U.; Gougoussis, C.; Kokalj, A.; Lazzeri, M.; Martin-Samos, L. *et al.* QUANTUM ESPRESSO: A Modular and Open-Source Software Project for Quantum Simulations of Materials. *Journal of Physics: Condensed Matter* **2009**, *21*, 395502.

72. Deslippe, J.; Samsonidze, G.; Strubbe, D. A.; Jain, M.; Cohen, M. L.; Louie, S. G. BerkeleyGW: A Massively Parallel Computer Package for the Calculation of the Quasiparticle and Optical Properties of Materials and Nanostructures. *Computer Physics Communications* **2012**, *183*, 1269–1289.
73. Felipe, H.; Qiu, D. Y.; Louie, S. G. Nonuniform Sampling Schemes of the Brillouin Zone for Many-Electron Perturbation-Theory Calculations in Reduced Dimensionality. *Physical Review B* **2017**, *95*, 035109.
74. Liu, F.; Wu, W.; Bai, Y.; Chae, S. H.; Li, Q.; Wang, J.; Hone, J.; Zhu, X.-Y. Disassembling 2D van der Waals Crystals into Macroscopic Monolayers and Reassembling into Artificial Lattices. *Science* **2020**, *367*, 903–906.
75. Bretscher, H. M.; Li, Z.; Xiao, J.; Qiu, D. Y.; Refaely-Abramson, S.; Alexander-Webber, J.; Tanoh, A. O.; Fan, Y.; Delport, G.; Williams, C.; Stranks, S. D.; Hofmann, S.; Neaton, J. B.; Louie, S. G.; Rao, A. The Bright Side of Defects in MoS₂ and WS₂ and a Generalizable Chemical Treatment Protocol for Defect Passivation. **2020**, 2002.03956. *Arxiv*. <https://arxiv.org/abs/2002.03956> (accessed May 7, 2021).

Supporting Materials For: Rational Passivation of Sulfur Vacancy Defects in Two-Dimensional Transition Metal Dichalcogenides

Hope Bretscher,[†] Zhaojun Li,^{†,‡} James Xiao,[†] Diana Yuan Qiu,[¶] Sivan Refaely-Abramson,[§] Jack A. Alexander-Webber,[†] Arelo Tanoh,[†] Ye Fan,[†] Géraud Delport,[†] Cyan A. Williams,[†] Samuel D. Stranks,[†] Stephan Hofmann,[†] Jeffrey B. Neaton,^{||,⊥} Steven G. Louie,^{||,⊥} and Akshay Rao^{*,†}

[†]*University of Cambridge, Cambridge, CB2 1TN, UK*

[‡]*Uppsala University, Uppsala, 751 20, Sweden*

[¶]*Yale University, New Haven CT, 06520, USA*

[§]*Weizmann Institute of Science, Rehovot, 76100, Israel*

^{||}*University of California Berkeley, Berkeley, CA, 94720, USA.*

[⊥]*Lawrence Berkeley National Laboratory, Berkeley, CA, 94720, USA*

E-mail: ar525@cam.ac.uk

Section 1: PL enhancement

To gain a greater understanding of the distribution of enhancement, we acquire PL maps, measuring the intensity of PL on different samples before and after different treatment methods. Using a PL microscope, we measure a PL spectrum at each point in real-space of a monolayer flake. After subtracting off a linear background to remove any contribution from scatter and detector noise, we then determine the maximum PL counts on each spectrum and

the energy at which this occurs. This is then plotted in a scatterplot, such that every point on a monolayer flake is represented by a corresponding point on the scatterplot. We acquire maps at two different times, first before further optimization of the PA+TFSI procedure (Fig.2a,top) in the main text, and after optimization (Fig. 1top).

In Fig.2a,top, we acquire PL maps on five different samples each of untreated, TFSI, and PA+TFSI samples. The measurements were performed on a Renishaw Invivo system, which can detect the PL of untreated samples. Both TFSI and PA+TFSI samples blueshift in their peak PL energy from 1.866 eV to 1.886 eV and 1.888 eV respectively, as well as narrowing of energy distribution from 0.012 eV to 0.006 and 0.005 eV respectively. PA+TFSI shows a greater enhancement in PL counts than TFSI alone. The improvement by PA+TFSI after more optimization of the treatment procedure is further shown in Fig. 1, in which the PL enhancement by PA+TFSI is much greater than that of TFSI alone, as the mean PL counts for PA+TFSI treatment is $\sim 4x$ TFSI alone. On this measurement, performed on the WITec Alpha system, the PL of the untreated sample was undetectable due to setup sensitivity.

Table 1: Statistics from scatter plots shown in Fig. 1,top and Main text, Fig. 2a,top.

Figure	Treatment	Mean energy (eV)	Mean counts	Max counts
1b,top	TFSI	1.880 ± 0.004	123 ± 19	378
1b,top	PA+TFSI	1.880 ± 0.004	595 ± 141	837
Main text Fig. 2a,top	Pristine	1.866 ± 0.012	25 ± 6	51
Main text Fig. 2a,top	TFSI	1.886 ± 0.006	200 ± 140	651
Main text Fig. 2a,top	PA+TFSI	1.888 ± 0.005	270 ± 20	924

PL enhancement and lifetime

We make similar spatial maps to measure the PL intensity and lifetime, as shown in Fig.2a and Fig. 1,bottom. In these maps, we acquire the PL intensity as a function of time, using a bandpass filter to select the photoluminescence. In Fig. 1, we make a scatter plot for two flakes of each treatment condition (one of which is shown in the main text, Fig.2b), plotting the PL intensity and lifetime. PA+TFSI samples have a narrower distribution and shorter

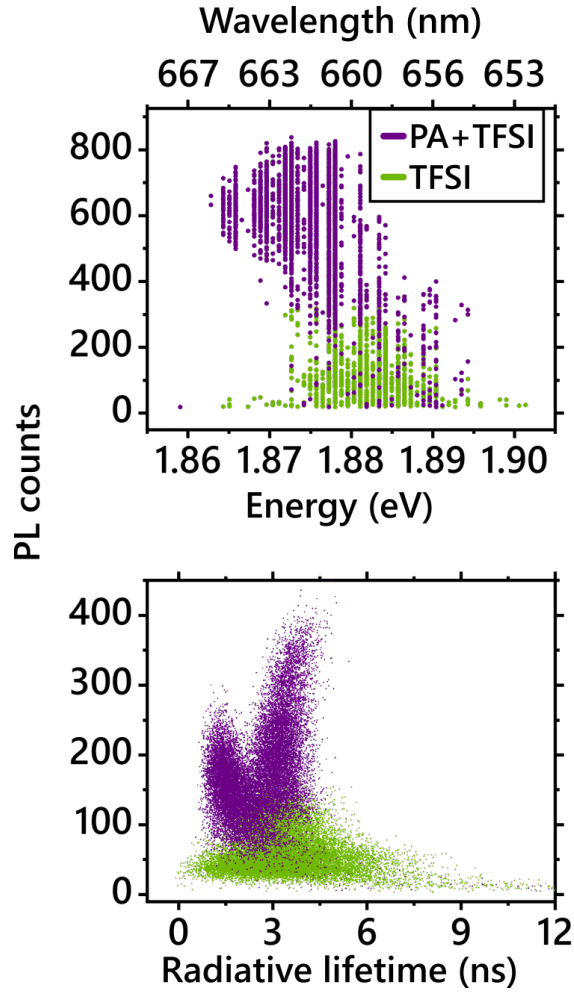


Figure 1: PL enhancement of TFSI and PA+TFSI treatment. Top: Emission energy *versus* maximum counts. With further optimization, PA+TFSI treatment shows PL $>2x$ as bright as TFSI alone. Bottom: The emission lifetime shortens and the distribution of emission lifetimes narrows with PA+TFSI treatment as compared to TFSI only. The bimodal distribution is because data shown comes from two different samples. Statistics are shown below.

lifetime than TFSI only samples, with statistics given in Table 2.

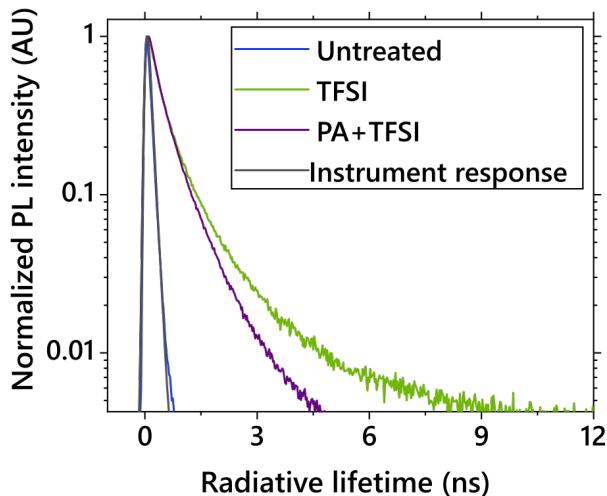


Figure 2: Illustrative time-correlated single photon counting (TCSPC) trace for untreated, TFSI, and PA+TFSI treated samples. The untreated sample’s PL is indistinguishable from the instrument response (shown in grey), so we can only conclude that the lifetime is shorter than 100 ps.

Table 2: Statistics from scatter plots shown in Fig. 1, bottom

Treatment	Mean lifetime (ns)	Mean counts
TFSI	3.45 ± 1.51	60.8 ± 30.4
PA+TFSI	2.5 ± 1.00	179 ± 65

Section 2: Pump-probe lifetime comparisons

To further compare the dynamics of different treatment conditions, we fit the decay lifetimes of the untreated and TFSI-treated samples with an fit function where an error function (to simulate the pump-induced rise in the signal) is convolved with a series of exponential decays,

$$\begin{aligned}
\frac{\Delta t}{t} = & y_0 + 0.5 \times A_1 \exp\left(\frac{s^2}{2\tau_1^2}\right) \times \exp\left(-\frac{t-t_0}{\tau_1}\right) \times \left(1 + \operatorname{erf}\left(\frac{t-t_0-s^2}{\tau_1 s \sqrt{2}}\right)\right) \\
& + 0.5 \times A_2 \exp\left(\frac{s^2}{2\tau_2^2}\right) \times \exp\left(-\frac{t-t_0}{\tau_2}\right) \times \left(1 + \operatorname{erf}\left(\frac{t-t_0-s^2}{\tau_2 s \sqrt{2}}\right)\right) \\
& + 0.5 \times A_3 \exp\left(\frac{s^2}{2\tau_3^2}\right) \times \exp\left(-\frac{t-t_0}{\tau_3}\right) \times \left(1 + \operatorname{erf}\left(\frac{t-t_0-s^2}{\tau_3 s \sqrt{2}}\right)\right) \quad (1)
\end{aligned}$$

In this equation, s is the instrument response, t_0 is time zero (when the pump and probe overlap), y_0 is a small y offset often from residual scatter, and A and τ correspond to the amplitude and decay time constant of each exponential decay. We use this equation to fit the decay kinetics for the A exciton bleach and defect bleach of the untreated and TFSI treated samples, as shown in Fig. 3, and with the corresponding fit parameters shown in table 3.

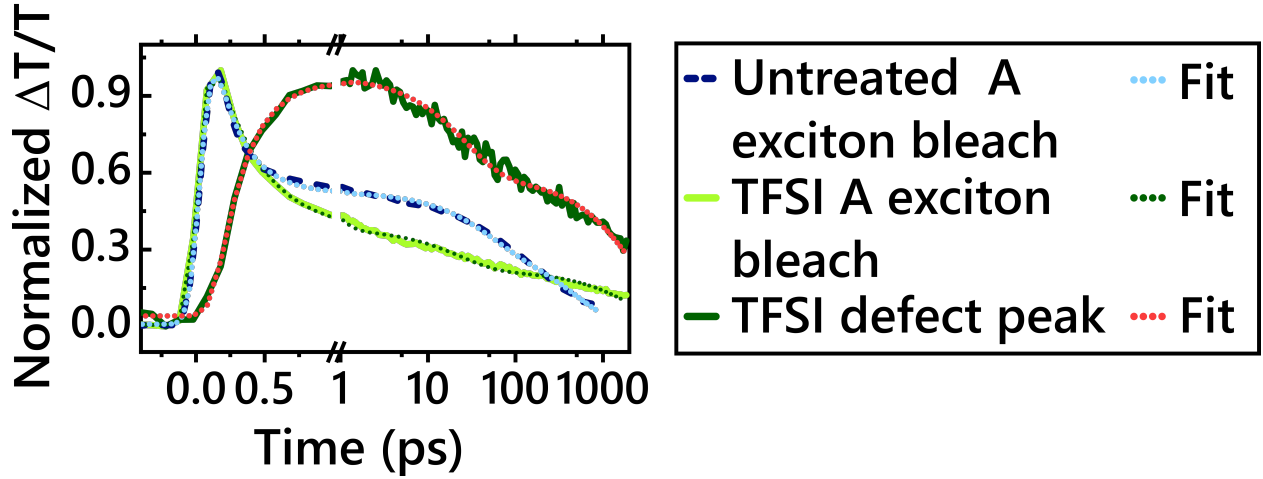


Figure 3: Pump-probe kinetics of the A exciton bleach and defect bleach. The dominant decay of the untreated sample is longer-lived than that of the TFSI treated sample. Fits are performed using equation 1

The A-exciton bleach of both the TFSI-treated sample exhibits a sub-picosecond decay component. After this initial decay, the bleach signal persists for a lifetime of tens of picoseconds. The subgap state (dark green) instead exhibits a sub-picosecond growth, before a similarly slow decay. By fitting the data with a fit function that includes an error function convolved with an exponential rise (to simulate the rise of the pulse), and a sum of exponen-

Table 3: Fit parameters using Eqn. 1 We first fit the A exciton bleach of both samples to determine the rise time (s), and then include this as a fixed parameter in the fitting process of the defect bleach. This allows us to capture the rise of the defect peak (which is not instrument response limited), as an exponential decay with a negative amplitude. All temporal units are in picoseconds.

	Untreated (bleach)	TFSI (bleach)	TFSI (defect)
A_1	0.85	0.94	-0.93
τ_1	0.21	0.34	0.21
A_2	0.21	0.16	0.39
τ_2	45.22	23.04	26.86
A_3	0.31	0.21	0.54
τ_3	490	2200	2300
Rise time (s)	0.07	0.07	0.07
Time zero (t_0)	0.03	0.02	0.12
Y offset (y_0)	0.01	0.01	0.04
χ_{red}^2	0.997	0.993	0.987

tial decays, we can give approximate time constants and amplitudes for each of these decay times (see 3 and 3). We note that the A exciton bleach of the TFSI-treated sample decays more significantly in the first 50 ps than the untreated sample. Simultaneous to its early decay is a rise of the defect state. We emphasize that these exact numbers vary to some degree sample to sample. Instead, we emphasize that this trend observed from comparing >5 untreated and TFSI treated samples.

Section 3: Exfoliation comparisons

To confirm that the effect of our chemical treatments is not due to our use of the gold exfoliation method, we compare the PL enhancement of sticky-tape exfoliated samples with those of gold-exfoliated samples, shown in Fig. 4. We exfoliate monolayer flakes using each method, and then measure the PL of the same monolayer flake before and after each treatment condition. We find that the TFSI and PA+TFSI treatments lead to significant enhancements in the original PL magnitude of each sample, confirming that our exfoliation method results in monolayers of similar quality as sticky tape exfoliated samples, as has been

previously found in previous works.^{53,74}

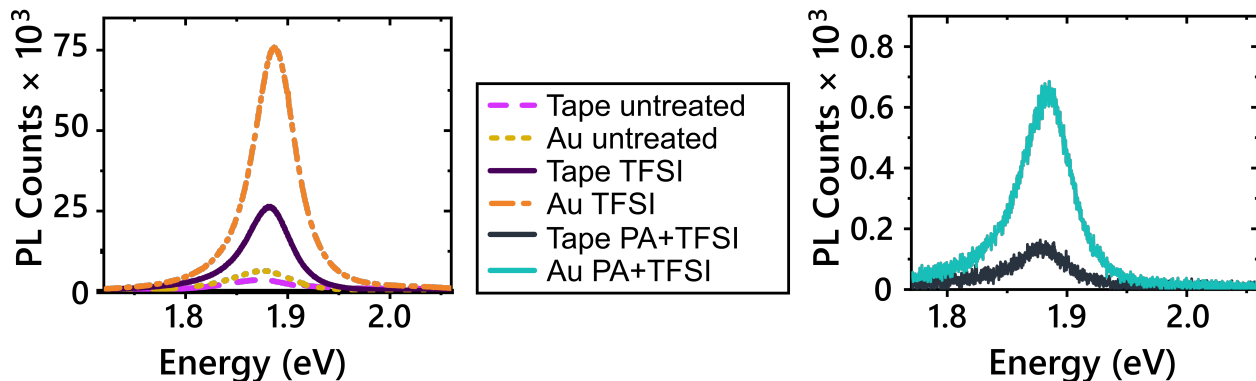


Figure 4: On the left, we plot the photoluminescence of a MoS₂ monolayer flake exfoliated using only sticky tape (tape), and using the gold exfoliation method (Au). Both the tape and Au samples exhibit a significant enhancement upon TFSI treatment. Because the PA+TFSI treated samples were even brighter and saturated the detector, we had to measure these under a higher power and different integration time, (shown on the right), in which the TFSI and untreated sample PL is undetectable. The chemical treatments show similar enhancements for the tape exfoliated samples as the gold samples.

Section 4: Subgap excitation pump-probe

For further evidence of subgap absorption, we perform pump-probe measurements exciting subgap. Theory predicts two subgap transitions. The transition from the occupied to unoccupied defect states, X_{D2} , is ~ 0.2 eV lower in energy than the A exciton transition. Theory predicts a second transition, X_{D1} , from the valence band to the subgap, unoccupied defect level, which is ~ 0.5 eV lower in energy than the A exciton transition. We therefore excite TFSI-treated samples at 1.67 eV and 1.38 eV (Fig 5), and both result in pump-probe spectra similar to those excited above-bandgap. In a and c, we show spectral dynamics of the TFSI-treated samples. In b and d, we plot the maximum $\Delta T/T$ at the A exciton bleach for three different powers, showing that the signal scales linearly with pump fluence and therefore is not a result of two-photon absorption. In an untreated sample, in e, even when exciting at the highest fluence of $120 \mu\text{J}/\text{cm}^2$, the signal was nearly negligible.

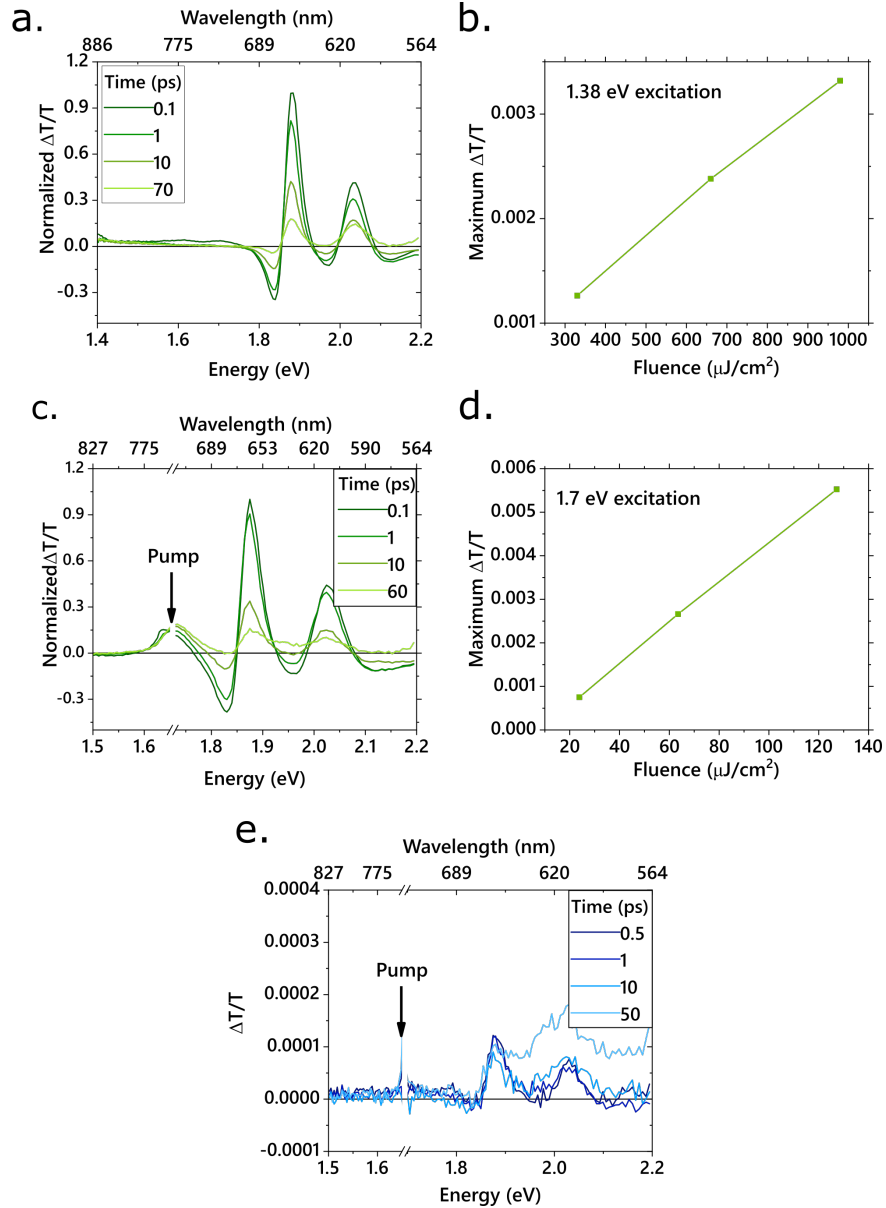


Figure 5: Pump-probe with sub-bandgap excitation. (A) Pump-probe of TFSI sample when excited at 1.7 eV with $\sim 60 \mu\text{J}/\text{cm}^2$ shows characteristic pump-probe spectrum and distinct subgap bleach. b. The maximum signal taken at the A exciton bleach (~ 1.88 eV) for a range of pump fluences shows a linear relationship between excitation fluence and signal magnitude. (c) Pump-probe of TFSI sample when excited at ~ 1.38 eV with $\sim 280 \mu\text{J}/\text{cm}^2$. (d) The maximum signal taken at the A exciton bleach (~ 1.88 eV) for a number of pump fluences shows a linear relationship between excitation fluence and signal magnitude. (e) When exciting an untreated sample at 1.7 eV and $\sim 140 \mu\text{J}/\text{cm}^2$ the signal is extremely weak.

Section 5: Pump-probe on PA treated sample

When measuring samples that have been treated with only a passivating agent, no subgap state is observed (Fig. 6).

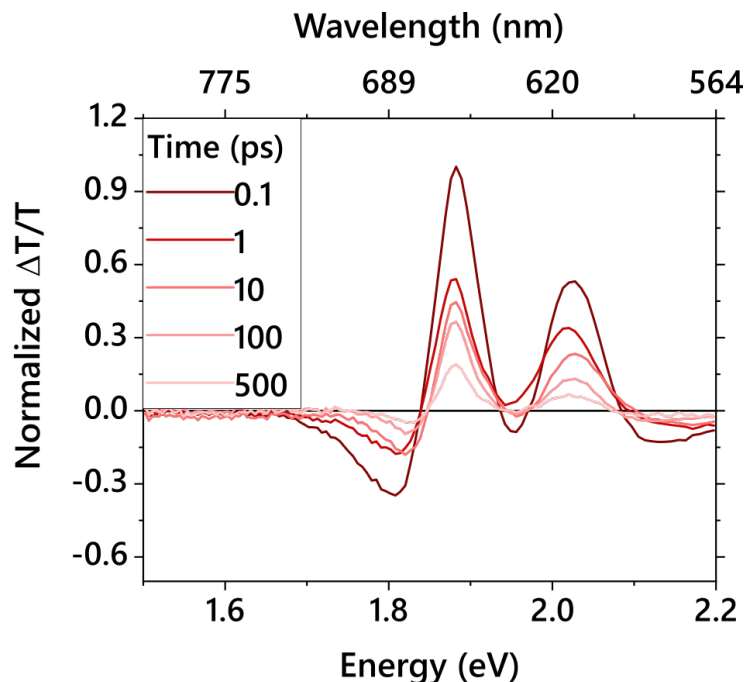


Figure 6: Pump-probe of passivating-agent only. Pump-probe measurements of passivating agent treated MoS₂ excited at 2.47 eV with $\sim 60 \mu\text{J}/\text{cm}^2$ shows no subgap state. Data is shown from a single sample, but has been measured on multiple monolayer flakes which display similar trends.

Section 6: Significance of treatment order

PA alone does not result in any increase in PL in MoS₂, and only a small increase in WS₂ (Fig. 7). The order of chemical treatments is significant for the enhancement of PL. A large enhancement is only observed when the passivating agent is applied first, and the superacid second. If the order is reversed, only a small increase is observed (Fig. 7).

Section 7: Untreated PL lifetime and instrument response

Untreated MoS₂ shows no significant difference from the instrument response time. We therefore conclude that its lifetime is below the instrument response time of 100 ps (Fig. 8).

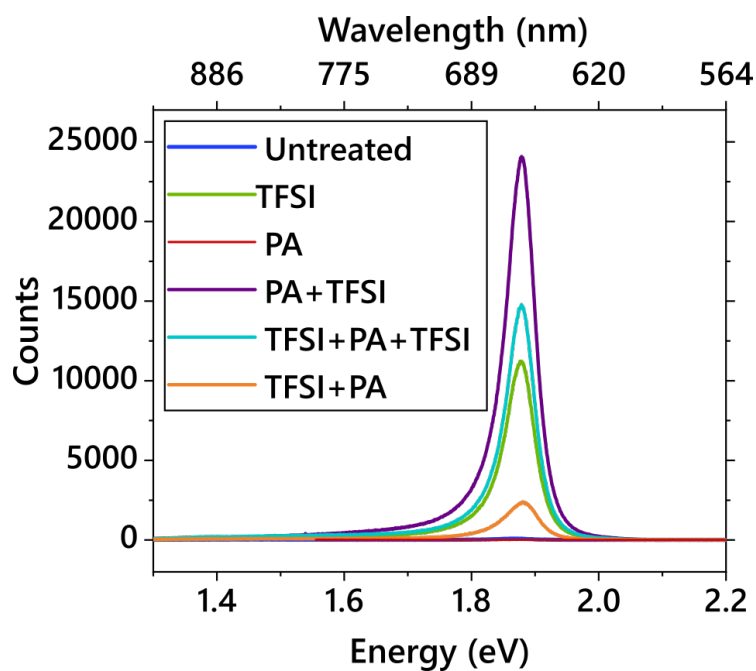


Figure 7: PL enhancement by treatment order. The passivation step must precede the TFSI to result in the largest PL enhancement. PA alone does not increase PL in MoS₂, whereas in WS₂ a small increase is observed (Fig.4b,bottom, main text). Data shown is a spectra representative of measurements taken over a number of samples, which show similar trends in magnitude of PL increase per treatment.

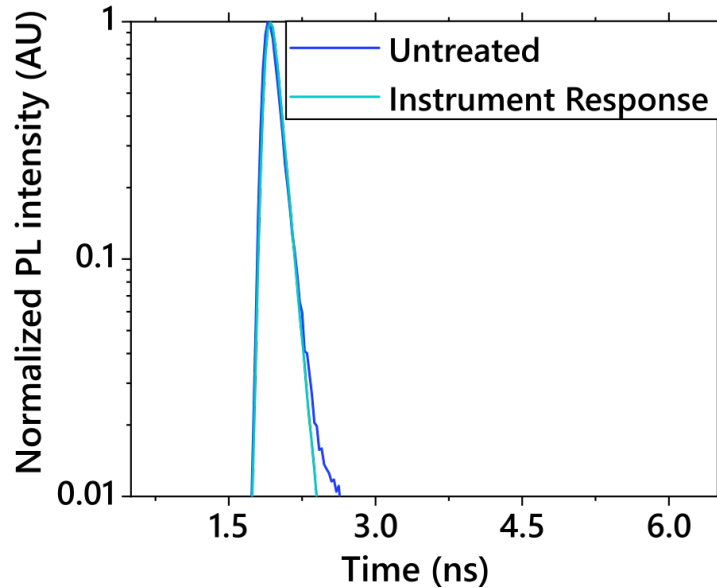


Figure 8: Instrument response of time-resolved PL measurement. Comparison of the time-resolved decay of the instrument response (green) and of the untreated sample (blue).

Section 8: Arrhenius equation and upconversion

The Arrhenius equation allows for the calculation of a rate coefficient given a temperature and activation energy. The equation is:

$$k = A \exp\left(-\frac{E_a}{k_B T}\right) \quad (2)$$

Where E_a is the activation energy, k_B is Boltzmann's constant, T , the temperature. The prefactor, A , can be given by the Raman modes of the system, in this case, A_{1g} at 408 cm^{-1} or the E_{2g} mode at 383 cm^{-1} .⁶⁹ The difference in energy between the defect state and the A exciton is $\sim 180 \text{ meV}$, however there is likely an energetic barrier to go from one state to another. We estimate the rate constant at room temperature, using the prefactor of the A_{1g} mode, and for a range of activation energies to account for possible energetic barriers.

At room temperature, the time constant for the transition from the defect state to the A exciton is on the order of picoseconds to nanoseconds. We measured a few nanosecond

Table 4: We use the Arrhenius equation to calculate the possible time constants for excitons to transition from trapped defects to the A exciton band edge given a range of energetic barriers. We assume the material is at room temperature and the known Raman modes are the prefactor.

Barrier height (meV)	Rate constant τ_U (ns)
180	0.095
225	0.320
250	0.84
300	5.8

lifetime at $8 \times 10^{-2} \mu\text{J}/\text{cm}^2$. Previous studies have measured ~ 10 ns measured at $\sim 4 \times 10^{-3} \mu\text{J}/\text{cm}^2$ ⁴ and 20 ns taken at a low fluence where exciton-exciton annihilation is not observed.⁴⁵ Given this range of 1-20 ns lifetime for radiative decay from the TFSI-treated A exciton, it is plausible that at room temperature, there is adequate energy for the band edge to be repopulated by thermal fluctuations on a timescale faster than decay from the defect states themselves. At 77 K, it has been shown that the radiative lifetime for the defect states is $\sim 4 \mu\text{s}$.⁴⁵

Section 9: GW-BSE calculation

We first performed density functional theory (DFT) calculations within the local density approximation (LDA)⁷⁰ using the Quantum-ESPRESSO code.⁷¹ The calculations were done on a 5x5 supercell arrangement of a MoS₂ monolayer with either one S vacancy or with a single O atom substituting of one of the S atom, following prior work.¹⁸ We used a plane-wave basis and norm-conserving pseudopotentials with a 125 Ry plane-wave cutoff. We included the Mo semi-core 4d, 4p, 4s, 5s and 5p states as valence states in our pseudopotential. The distance between repeated supercells in the out-of-plane direction was 15 Å. We relaxed the geometry within DFT and used DFT charge density as a starting point for our GW and Bethe Salpeter equation (GW-BSE) calculations.

Our GW calculations are performed with the BerkeleyGW code⁷² using the generalised

plasmon-pole model,⁴⁹ an energy cutoff of 25 Ry for the planewave components of the dielectric matrix, and a nonuniform k-point sampling corresponding to a 30x30 uniform k-grid.⁷³ We included 4000 unoccupied states in the sum over empty states in the self energy and polarizability and tested the convergence with respect to unoccupied states by comparing to a calculation using up to 20,000 effective states obtained by averaging high-energy states within a small energy window. We find that these parameters converge the relative quasiparticle energies for the defect and pristine states at the K point to within 100 meV.

The BSE was also solved with the BerkeleyGW code.^{72,51} We diagonalise the BSE Hamiltonian within the Tamm-Dancoff approximation with 10 valence and 10 conduction bands. The clustered sampling interpolation (CSI) scheme⁷³ was used to interpolate a nonuniform k point sampling to a uniform k-grid of 18x18x1 k points. A 5 Ry cutoff was used for the planewave components of the dielectric matrix used in the BSE. Spin orbit coupling was added as a perturbation. We find that these parameters converge the calculated exciton excitation energies up to 200 meV.

Discussion of substitutional oxygen and sulfur vacancies

Based on these results and previous literature, we propose two possible reasons that the PLQY can be increased by TFSI-treatment. First, in untreated MoS₂, *n*-doping may result in the predominance of trions which quench the PL emission.^{26,39,61} When TFSI, functioning as a Lewis acid, is applied on the surface of MoS₂, the excess electrons of MoS₂ are removed, leading to a shift in threshold voltage observed in transistors as well as the blueshift in the PL. As the samples become more intrinsic, neutral excitons dominate leading to an increase in PL. Another possible explanation is that oxygen substitutions are the dominant defect, rather than sulfur vacancies, and that these create local sites with metallic character, providing a route for non-radiative recombination that quenches the PL. Given that the samples are known to be *n*-doped,^{26,40–42} it is possible that both oxygen substitutions, and

n-doping, both reduce the overall PLQY.

The *n*-doping explanation (as the dominant factor contributing to a low QY) is not fully satisfactory given our experiments and the current literature. First, a number of studies report significant reductions in *n*-doping and large Fermi-level shift, but observe only modest increases in PL.^{29,31,33} We have similarly found that molecular *p*-dopants lead to modest gains in PLQY. If the Fermi-level shift is as significant and the low PL is predominantly caused by *n*-doping, we would expect molecular dopants to see a large increase in PL. Second, we would also expect that molecular doping may result in a subgap absorption state, but this has not been observed.

However, we have struggled to find any evidence of the presence of oxygen substitutions. Indeed the identification of oxygen substitutions is extremely challenging and requires the use of UHV based techniques like STM, which are not compatible with the wet chemical passivation methods used here. Thus, our experimental results and their close correspondence with theory predictions supports the idea that the TFSI treatment results in a sulfur vacancy, and the PA+TFSI treatment passivates this. However, the nature of these sulfur vacancies in untreated materials, if they are filled with oxygen or *n*-doping will need future experimental and theoretical study.